Peer reviewed version

License (if available):
CC BY-NC

Link to published version (if available):
[10.1002/we.1900](#)

[Link to publication record in Explore Bristol Research](#)
PDF-document

Aerodynamic and aeroacoustic performance of airfoils with morphing structures

Qing Ai [1], Mahdi Azarpeyvand [2], Xavier Lachenal [1], Paul M.Weaver [1] .

[1] Advanced Composites Centre for Innovation and Science (ACCIS), University of Bristol, Bristol BS8 1TR, UK
[2] Department of Mechanical Engineering, University of Bristol,Bristol BS8 1TR,UK

ABSTRACT

Aerodynamic and aeroacoustic performance of airfoils fitted with morphing trailing edges are investigated using a coupled structure/fluid/noise model. The control of the flow over the surface of an airfoil using shape optimization techniques can significantly improve the load distribution along the chord and span lengths whilst minimising noise generation. In this study, a NACA 63-418 airfoil is fitted with a morphing flap and various morphing profiles are considered with two features that distinguish them from conventional flaps: they are conformal and do not rely on conventional internal mechanisms. A novel design of a morphing flap using a zero Poisson's ratio honeycomb core with tailored bending stiffness is developed and investigated using the finite element model. While tailoring the bending stiffness along the chord of the flap yields large flap deflections, it also enables profile tailoring of the deformed structure which is shown to significantly affect airfoil noise generation. The aeroacoustic behaviour of the airfoil is studied using a semi-empirical airfoil noise prediction model. Results show that the morphing flap can effectively reduce the airfoil trailing edge noise over a wide range of flow speeds and angles of attack. It is also shown that appropriate morphing profile tailoring improves the effect of morphing trailing edge on the aerodynamic and aeroacoustic performance of the airfoil.

KEYWORDS
airfoil self-noise; morphing trailing edge; zero Poisson's ratio honeycomb core; stiffness tailoring.

1. INTRODUCTION

The growing interest in sustainable energy, including that from wind, has reshaped the energy market over recent decades and wind turbine manufactures are facing the trend to upscale the turbine blade size due to economic drivers.[1] To improve power production, the size of turbines (tower height and blade length) has increased significantly recently. The increase in the size of the tower and blade, in turn, has brought new challenges, such as tower load control, turbine lift enhancement and mitigation, gust load alleviation and fatigue loads reduction.[2,3] At the same time, concerns have been raised regarding low frequency noise from wind farms and its potential impact on public health. It is of note that wind turbine noise is currently a major hurdle for the construction of new wind farms around urban regions. In order to maintain efficiency of turbine control systems and reduce noise emission from wind turbines, various active control devices, enabling local turbine load control and noise reduction, have been proposed and studied in combination with conventional pitch and yaw control systems.[2–12] Regarding noise reduction, however, it is important to understand the airfoil noise generation mechanisms, particularly that from the trailing edge (TE). In the following subsections, we explain the TE noise,[13–16] the existing airfoil noise reduction techniques,[17–27] and finally discuss the application of morphing technology for airfoil flow control and noise reduction purposes.

1.1. Airfoil aerodynamic noise

Noise generated by wind turbines comes from both mechanical and aerodynamic sources with the latter considered dominant.[13] The aerodynamic noise generation mechanism has been extensively studied and is classified into three main groups:[13] (1) the steady thickness noise due to the rotation of blades and unsteady noise due to the passage of the blades through the tower wake, (2) the inflow turbulence noise generated by the interaction of blades with the atmospheric turbulence of incoming flow, and (3) the airfoil self-noise resulting from the interaction of the airfoil blade and the turbulence produced within its boundary layer.

When an airfoil encounters a smooth non-turbulent inflow, the airfoil self-noise dominates the total noise generated by the airfoil.[14] In particular, the TE noise, due to the interaction of the TE and the boundary layer over the surface of the blade, has been identified as the main source of airfoil self-noise particularly at small angles of attack.[13,14] It is worth noting that if the incoming flow is turbulent, the inflow turbulence noise is regarded as the main component of noise at low frequencies.[13,16] In this article, however, we focus on TE noise generation.

Different flow control devices have been utilized to improve aerodynamic and aeroacoustic performance of airfoils.[28] Aircraft wing flaps are the most popular devices used by the aerospace industry to control lift and drag produced by the wing during take-off and landing. Several passive methods have been developed to reduce airfoil noise, such as trailing edge serrations,[17–21] trailing edge brushes,[22,23] porous trailing edges,[24,25] and airfoil shape optimization.[26,27] Sawtooth serrations have been adopted as a passive device to reduce TE noise.[17–21] Howe[20] theoretically investigated the noise generated by a flat plate airfoil with serrated TE and showed that TEs with periodic serrations can potentially reduce the radiated noise. Gruber et al.[18] and Oerleman et al.[21] experimentally measured the noise level of airfoils fitted with TE serrations and noise reduction of up to 3.2 dB was obtained over a large frequency range. Brushes have also been used to reduce the TE noise.[22,23] Experiments by Herr et al.[22] and Finez et al.[23] showed that the TE noise level can be decreased by in excess of 10 dB over a wide frequency range with brushes integrated into the airfoil TE. The use of porous treatments near the TE to reduce noise radiation has also been considered in the literature.[24,25] More recently, Geyer et al.[25] conducted an experimental survey on a set of airfoils made of different porous materials and obtained a noise reduction of up to 10 dB over the low to medium frequency range. However, the main objective of airfoil treatments is to reduce low frequency noise, as the sound waves at high frequencies attenuate over relatively short distances.

Airfoil shape optimization is extensively used to improve aerodynamic performance and control noise radiation.[26,27] Gocmen et al.[26] carried out optimization designs on six different wind turbine airfoils and showed that with geometrical optimization applied to the airfoils, low noise level and high lift-to-drag ratios can be achieved. Jones et al.[27] developed a parallel genetic algorithm methodology and generated a family of two-dimensional airfoils, addressing the compromises between aerodynamic efficiency and noise reduction. Based on the findings in Refs. [26, 27], airfoil shape optimization has shown a great potential for controlling noise generation without affecting the aerodynamic performance of the airfoil. It is important, however, to note that airfoil optimization, including single- and multi-objective optimization, is usually performed using only one or limited number of operating conditions encountered by wind turbines or helicopter rotor blades.[26,27] Airfoil performance becomes compromised when the operation condition is beyond the optimization design scope. Compared to the passive airfoil optimization technique, active control methods such as morphing trailing edges,[3–5] combined with pitch and yaw operations, could respond adaptively to the varying flow conditions with an appropriate control strategy and thereby improve the capability of turbine load and noise control. A variety of active flow control methods have also been investigated recently for wind turbine blades and helicopter rotors, such as microtabs,[2] morphing structures,[3–5,29] aileron flaps[6–11] and boundary layer suction[12] and it has been shown that aerodynamic performance and noise emission of the airfoil can be significantly improved. Implementing local active control surfaces could alleviate excessive loads including extreme structural loads and fatigue loads, which leads to the reduction of turbine costs by reducing materials and maintenance cost and increasing the overall turbine reliability and lifetime.[2] Of particular interest in active control methods are morphing aero-structures, due to their light weight and enhanced aerodynamic efficiency compared to aileron flaps.[4,30–32] Many morphing concepts for aero-structures have been developed in recent years and several reviews are available.[30–32]

1.2. Airfoil morphing structures

A morphing TE actively changes its shape through structural deformation instead of rigid body motion and thereby offers continuously smooth aerodynamic surfaces without slots, gaps and cavities, *i.e.* they are conformal, which are considered as dominant sources of cavity noise and side edge noise. In order to develop an applicable morphing device, several conflicting structural requirements, such as deformability, load-carrying capability and light weight, have to be reconciled.[33] In particular, a high flexural stiffness/ in-plane stiffness ratio is required for aero-structures to carry pressure load and reduce the actuation forces. In order to address the challenges, several concepts have been proposed and studies.[4,5,33–35] The highly anisotropic nature of composite materials and structures, such as honeycomb cores, makes them ideal candidates for morphing structures.[36–38]

In the smart wing program led by the Northrop Grumman Corporation, an adaptive TE control surface was developed and tested in wind tunnel by Bartley-Cho et al.[34] The hingeless control surface consisted of three main parts: (1) an elastomeric (silicone) outer skin, (2) a flexible honeycomb core and (3) a center composite leaf spring. The silicone skin provided a smooth and continuous surface capable of undergoing large strain up to 600%. The flexible honeycomb core supporting the silicone skin provided the out-of-plane stiffness for the structure and also enabled a low actuation force. The honeycomb core and outer skin were attached to the center glass fibre laminate, which acted as a hard point, stabilizing the chordwise shape. The wind tunnel test showed that the morphing TE segment was able to undergo deflection up to 20°.[34] It was also found that the actuation force can be further reduced by changing the honeycomb core material from aluminium

to a nonmetallic material, such as a phenolic or aramid core. Daynes and Weaver[4,5] proposed a morphing TE device using a honeycomb core, a Carbon Fibre Reinforced Plastic (CFRP) upper skin and a silicone lower skin. The CFRP upper skin offered a smooth upper surface and supported the attached honeycomb core. The flap was actuated by a CFRP actuator rod. Experimental results showed that in non-stall flow regimes the morphing deflection yielded a lift coefficient change of about $0.05/deg$ and the flap was successfully actuated using a conventional off-the-shelf servomotor.

The anisotropic properties of cellular solids, including honeycomb cores and foams, provide high out-of-plane stiffness and low in-plane stiffness, addressing the structural requirements of an ideal morphing structure. Compared to traditional materials, honeycomb cores present wider mechanical property tailorability using different materials and geometries,[35] which enables its application in morphing structures. It is worth noting that, however, when considering a one-dimensional morphing device using a honeycomb core, such as a chord-wise morphing flap, the anticlastic effect due to the Poisson's ratio of honeycomb core causes an unwanted curvature in the non-morphing direction *i.e.* span-wise. To overcome this issue, solutions were presented, such as slicing the core into rows[4] and using zero Poisson's ratio (ZPR) honeycomb cores.[36–38]

Olympio *et al.*[36,37] investigated the mechanical properties of cellular solids with ZPR and used them in one-dimensional morphing structures. Results showed that cellular solids with ZPR, such as an accordion and hybrid flex cores, can provide similar in-plane axial stiffness and strain capabilities compared to the regular, hexagonal cell, honeycomb core without the associated anticlastic effect. Bubert *et al.*[38] proposed a one-dimensional morphing aircraft skin using a honeycomb core with ZPR and an elastomeric matrix composites skin. It was shown that 100% global strain could be achieved with the demonstrator. Chen *et al.*[39] designed and manufactured a curved cellular SILICOMB structure with ZPR using the Kirigami techniques. The relation of the stiffness of the curved cellular structure and the geometry parameters of its representative unit cell was investigated. Experimental results suggested that the large deformation and shape recovery capability of the core, together with the tunable mechanical properties, make it a good candidate for morphing applications.

In this paper, the concept of reducing the airfoil noise and improving the aerodynamic performance of the airfoil using a morphing TE is investigated. It is particularly important to simultaneously consider the aerodynamic efficiency and noise reduction for wind turbine applications as compromising the lift over the noise level can lead to the loss of the efficiency of the wind turbine. Of particular interest here is to study the effects of changes in shape of the deformed morphing TE on both aerodynamic and aeroacoustic performance of the airfoil. However, the focus is on the effect of morphing TE on airfoils encountering non-turbulent incoming flow. A novel morphing TE concept, using a bending stiffness tailored honeycomb core with ZPR, is proposed as an example. Optimization studies are conducted, using a Matlab script (MATLAB 7.14, The MathWorks Inc., Natick, MA, USA, 2012), which couples a two-dimensional Finite Element Model (FEM) to determine the mechanical properties of the morphing TE, an interactive airfoil aerodynamic properties program, Xfoil,[40] and the BPM (Brooks, Pope and Marcolini)[14] model to predict the far-field noise from the airfoil. Details of the design and analysis of the novel morphing TE concept are described in the following sections.

2. AIRFOIL NOISE PREDICTION

The complex nature of airfoil self-noise generation mechanism makes the accurate prediction of noise level difficult. Different empirical and semi-empirical models have been developed for this purpose.[14,41] Schlinker *et al.*[41] proposed an empirical noise prediction model relying on the flow properties in the boundary layer around the TE. By separating the airfoil self-noise into different sources, Brooks *et al.*[14] developed a semi-empirical model, known as the BPM model, which uses the boundary layer displacement thickness (δ^*) at the TE as input. For more accurate TE noise predictions, the unsteady fluctuating surface pressure data must be used,[42,43] which requires precise surface pressure measurements or high quality computational fluid dynamic calculations (CFD). The most popular methods used in recent literature are based on computational fluid dynamics or computational aeroacoustics.[41,43–46] The CFD-based models are, however, computationally expensive and can not be used for optimization purposes. In this paper, the semi-empirical BPM model is used to calculate the noise level of the airfoils fitted with a morphing TE. XFoil has been widely used in literature for its validity and capability to perform two dimensional airfoil aerodynamic calculations[16,26,29,50] and is used in this research to calculate the airfoil boundary layer properties including the boundary layer displacement thickness at the TE which is then used as input for the BPM model. In the BPM model, airfoil self-noise components are treated separately and the total noise level is computed by incoherently adding these components. The main noise components are as follows:[14]

- Turbulent boundary layer and trailing edge interaction noise (TBL-TE);
- Separation stall noise;
- Laminar boundary layer-vortex shedding noise;
- Tip vortex formation noise;
- Trailing edge bluntness- vortex shedding noise.

3

Semi-empirical expressions have been developed for each noise component.[14] For the cases considered in this article, only the TBL-TE noise and separation stall noise are relevant and described in detail.

$$SPL_{TOT} = 10 \log(10^{SPL_\alpha/10} + 10^{SPL_s/10} + 10^{SPL_p/10}), \tag{1}$$

where SPL_α is the stall noise and SPL_s, SPL_p refer to the noise due to the interaction of the boundary layers on the suction and pressure sides of the airfoil with the TE, and are given by

$$SPL_s = 10 \log(\frac{\delta_s^* M^5 L \bar{D}_h}{r_e^2}) + A(\frac{St_s}{St_1}) + (K_1 - 3), \tag{2}$$

$$SPL_p = 10 \log(\frac{\delta_p^* M^5 L \bar{D}_h}{r_e^2}) + A(\frac{St_p}{St_1}) + (K_1 - 3) + \Delta K_1, \tag{3}$$

$$SPL_\alpha = 10 \log(\frac{\delta_s^* M^5 L \bar{D}_h}{r_e^2}) + B(\frac{St_s}{St_2}) + K_2, \tag{4}$$

where δ_s^* and δ_p^* denote the boundary layer displacement thickness on the suction and pressure sides, respectively, and M is the Mach number of the flow, r_e is the distance between the airfoil trailing edge and the observer, c is the chord length and L is the span-wise extent wetted by the flow (see Figure 1). A detailed description of the BPM model and the parameters used can be found in Ref.[14]. The directivity factor $\bar{D}_h$ is defined using the following empirical relationship:[14]

$$\bar{D}_h(\Theta, \Phi) \approx \frac{2 \sin^2(\Theta/2) \sin^2(\Phi)}{(1 + M \cos(\Theta))[1 + (M - M_c) \cos(\Theta)]}, \tag{5}$$

where $M_c = 0.8 \cdot M$,[14] is the convection Mach number, and the polar and azimuthal angles,(Θ, Φ), are shown in Figure 1.
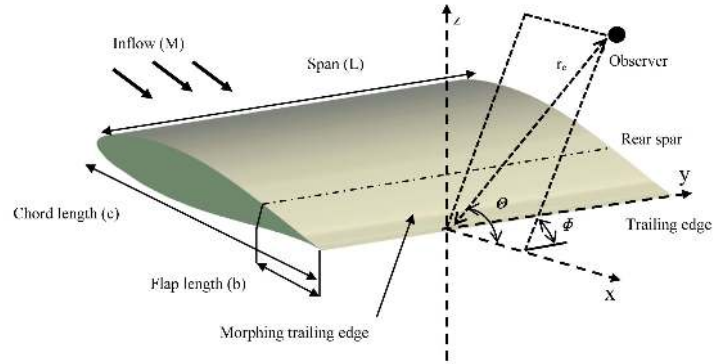

Figure 1. An airfoil fitted with a morphing trailing edge

3. THE NOVEL MORPHING TRAILING EDGE CONCEPT

Morphing structures in wind turbines[4] and aircrafts[31] have been investigated for flow and noise control purposes in recent years and this section describes design of a novel morphing TE device. In this paper, the NACA 63-418 airfoil with a chord length of 1.3 m, which is comparable to a 70% blade radial location of a generic Vestas V90 wind turbine,[5] is chosen for this research. A 20% (b/c) morphing TE, 260 mm, is fitted on the airfoil considering airfoil structure design requirements

and it also allows use of the morphing flap developed by Daynes *et al.*[4] as a benchmark case to qualify the benefits of the proposed morphing TE using a bending stiffness tailored core.

The novel morphing device consists of : (1) a CFRP upper skin, providing bending stiffness to the structure, (2) a bending stiffness tailored honeycomb core with ZPR, to avoid unwanted anticlastic curvature and reinforce the through-thickness stiffness of the flap, and (3) a silicone membrane as the lower skin, as shown in Figure 2. A push/pull CFRP rod is constraint to the bottom surface of the core using Polytetrafluoroethylene (PTFE) U-shaped hooks embedded within the honeycomb core at the bottom surface, allowing the rod to freely move in and out of the flap along the bottom surface, but not move in the thickness direction, transferring the loads from the rod to the honeycomb core.[4] The proposed airfoil TE, on one hand, undergos large deformations for flow control, and, on the other hand, provides changes in shape of the morphed TE for noise reduction purpose due to careful tailoring of the bending stiffness of the honeycomb core in the chord-wise direction. To properly study the efficiency of the proposed morphing TE and its bending stiffness tailored honeycomb core, three parameters are monitored: (1) airfoil aerodynamic performance (*i.e.* lift and drag coefficients), (2) the far-field noise level, and (3) the required actuation force. These considerations are further discussed in Section 4.
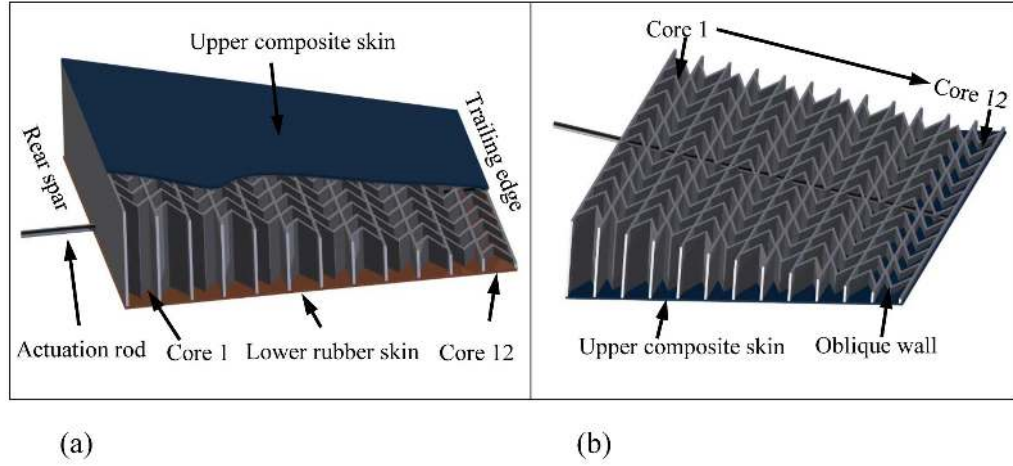
Figure 2. Three-dimensional geometry model of the honeycomb core: (a) top view of the morphing trailing edge; (b) bottom view with the lower skin and PTFE hooks removed for clarity

3.1. The ZPR honeycomb core design

The honeycomb core configuration with ZPR proposed by Bubert *et al.*[38] (Figure 3) is adopted in this article. The mechanical properties of the honeycomb core, such as the in-plane modulus, E_x, and the through-thickness Young's modulus E_z, are dependent on the material properties and core geometry and are determined using cellular solids theory, as per Gibson and Ashby.[35]

The deflection of cell-wall AB, as shown in Figures 3 and 4, due to the axial force F_x can be calculated using:[35,47]

$$\delta = \frac{F_x l^3 \cos\theta}{12E_0 I},$$

(6)

where E_0 is the Young's modulus of the honeycomb core material, $I = dt^3/12$, is the second moment of area of section AB, d is the local thickness of the core, t refers to the oblique wall thickness and l is the oblique wall length. The equivalent stress and strain of one representative cell unit, σ_x and ϵ_x can be calculated by:

$$\sigma_x = \frac{F_x}{Dd},$$

$$\epsilon_x = \frac{2\delta\cos\theta}{h}.$$

(7)

The equivalent in-plane Young's modulus of the honeycomb core in the X direction can be calculated as,
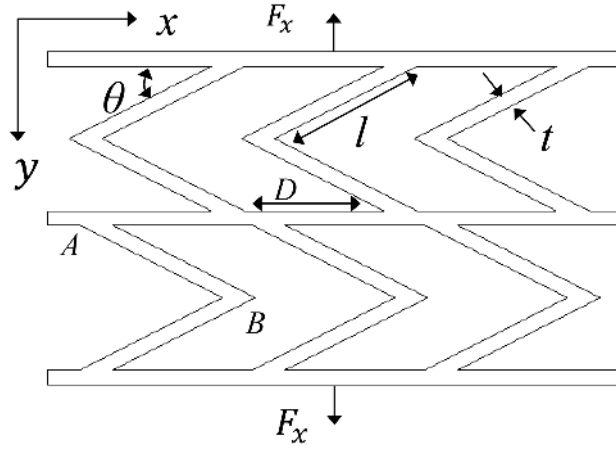
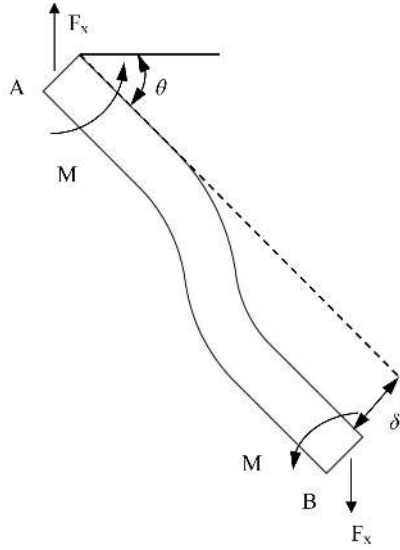**Figure 3.** Unit cell geometry definition of the honeycomb core substructure[38]

Figure 4. Deflection of section AB under tensile load

$$\frac{E_x}{E_0} = (\frac{t}{l})^3 \frac{\sin\theta}{\frac{D}{l}\cos^2\theta}. \tag{8}$$

The out-of-plane properties of the core are generally larger and more complex to determine than the in-plane ones. With a low density assumption, the through-thickness Young's modulus of the core, scaled by the area of effective load bearing section, is given by:[35]

$$\frac{E_z}{E_0} = \frac{t}{D\sin\theta}. \tag{9}$$

3.2. Mechanical characteristics of the ZPR honeycomb core

In order to verify the analytical model of the core Young's modulus, three dimensional FEM using ABAQUS (ABAQUS 6.12, Dassault Systems Inc., VV, France) was done and experimental tension tests also performed on the manufactured

Table I. Different honeycomb core column thickness distribution cases (mm)

Core	Case 1	Case 2	Case 3	Case 4	Case 5	Case 6	Case 7	Case 8	Case 9	Case 10
Core 1	2	2	2	2	1.5	1	0.5	1	0.5	0.5
Core 2	2	2	2	2	1.5	1	0.5	1	0.5	0.5
Core 3	2	2	2	2	1.5	1	0.5	1	0.5	0.5
Core 4	2	2	1.5	1	1.5	1	0.5	1	1.5	1
Core 5	2	1.5	1.5	1	1.5	1	0.5	1.5	1.5	1
Core 6	2	1.5	1.5	1	1.5	1	0.5	1.5	1.5	1
Core 7	2	1.5	1	1.5	1.5	1	0.5	1.5	1	1.5
Core 8	2	1.5	1	1.5	1.5	1	0.5	1.5	1	1.5
Core 9	2	1	1	1.5	1.5	1	0.5	2	1	1.5
Core 10	2	1	0.5	0.5	1.5	1	0.5	2	2	2
Core 11	2	1	0.5	0.5	1.5	1	0.5	2	2	2
Core 12	2	1	0.5	0.5	1.5	1	0.5	2	2	2

samples. The honeycomb core samples, with geometry parameters of $h = 20\ mm, D = 21\ mm, \theta = 30°$ and four different oblique wall thickness, t, (0.5 mm, 1 mm, 1.5 mm, and 2 mm), were prepared using a Stratasys machine (Stratasys Inc., USA) employing a fused deposition modelling process. The core material used is the Stratasys ABS plastic and due to the nature of the manufacture method, the ABS plastic parts present orthotropic mechanical properties: $E_{1,2} = 2016$ MPa, $\nu_{1,2} = 0.43$, $E_3 = 1530$ MPa , $\nu_3 = 0.41$[48] (*1, 2* denote the in-plane material properties and *3* refers to the through-thickness direction). The shear modulus of the material is estimated using the geometric mean of orthotropic moduli ($E_{eq} = 1756$ MPa, $\nu_{eq} = 0.42$), leading to $G_{eq} = 618.5$ MPa.[48] Tensile tests were conducted on the rapid prototyped samples using an Instron 3343 testing system (Figure 5). The resulting stiffness are compared with the analytical expression, Eq. 8, as shown in Figure 6. It can be seen that for the chosen design cases, the analytical model is in good agreement with the results from both the experimental test and FEM. Therefore, in the following section, the analytical model is used for prediction of the mechanical properties of different honeycomb cores used in the morphing TE designs.

Figure 5. Tensile test of the rapid prototyped honeycomb core
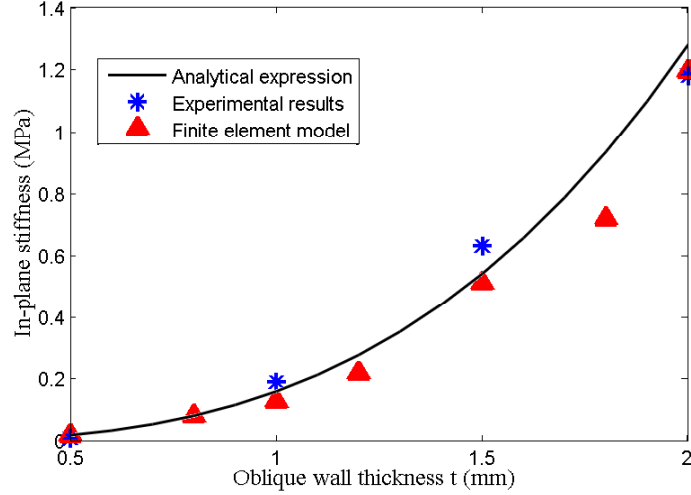
Figure 6. In-plane Young's modulus of the honeycomb core in the morphing direction ($h = 20mm, D = 21mm, \theta = 30°$)

3.3. Finite element model of the morphing trailing edge

A two-dimensional non-linear ABAQUS FEM of the morphing TE has been prepared to evaluate the mechanical properties of the morphing TE (Figure 2). After a mesh convergence analysis, the morphing flap is modelled using a 9×85 mesh with the elements dimension decreasing towards the trailing edge. In the FEM, the upper and lower skins are modelled using B21 beam elements with rectangular cross section. The CFRP upper skin has a layup of $[90/0/90]$ with $0°$ in the morphing direction and the overall thickness of the laminate is $0.6~mm$. The equivalent mechanical properties of the CFRP upper skin is calculated using the classical laminate theory.[49] The lower silicone skin has a thickness of $2~mm$ with a Young's modulus of 1 MPa.[5] To ease the manufacture, the morphing TE is approximated, with limited error, to a triangular section, as shown in Figure 2. The thickness of the honeycomb core decreases from $70~mm$ at its interface with the blade (referred to as the flap rear spar) to zero at the trailing edge (Figure 2). The honeycomb core consists of 12 rows of oblique walls and each row is numbered from 1 to 12 (Core 1 to Core 12), as shown in Figure 2. The pitch of the rows, delimited by ribs, is set at 20 mm in the chord-wise direction. The honeycomb core is modelled with CPS4R quadrilateral elements for most parts and triangular elements are used in the trailing edge section. The CFRP actuation rod is $320~mm$ long with a circular cross section of $1~mm$ diameter. The rod has a longitudinal Young's mosulus of $E_x = 140$ GPa and a lateral Young's modulus of $E_y = 10$ GPa and in the FEM is modelled with B21 elements. The flap section is then clamped at the rear spar (Figure 2). In order to obtain different morphing profiles for the same trailing edge displacements, ten different honeycomb core design cases are shown for a preliminary optimization, as listed in Table I.

4. RESULTS AND DISCUSSIONS

In this section, the aerodynamic and aeroacoustic performance of airfoils fitted with morphing trailing edges are studied using the XFoil/BPM model developed in Section 2 and discussed in this section. The morphing flap device developed by Daynes *et al.*[4,5] is investigated as a benchmark case, labelled as Case 0 henceforth. Results and discussions are presented in detail in the following sections. Considering the operating envelope of the V90 turbine used herein, a parametric study has been carried out for a variety of flow velocities (30 ms^{-1} and 50 ms^{-1}), morphing TE deflection angles ($-10°$ to $10°$) and angles of attack ($0°$ to $6°$). The deflection angle is defined in radians as arcsine of the ratio between the trailing edge deflection and the flap length[4] (positive/negative angles mean downwards/upwards deflection). In the following sections, only two representative morphing angles, $\beta = 8°$ and $-6°$, are chosen for downwards and upwards deflection respectively for reasons of clarity.

4.1. Mechanical response of the morphing trailing edge

The amount of the actuation force required for a given TE displacement can be affected by the deformation shape of the morphing TE and its slope distribution along the flap chord, b, resulting from the bending stiffness variation in the honeycomb core. With the two-dimensional FEM, different morphing flap designs using the ten typical honeycomb

core design cases in Table I are studied for the actuation requirement properties. As shown in Figure 7, by varying the bending stiffness distribution of the honeycomb core in the chord direction, the actuation force required for the same TE displacement can significantly change. Case 9 and Case 10 have the lowest actuation requirements of all the considered cases including Case 0,[4] as they possess the smallest stiffness at the rear spar region (0.5 mm oblique wall thickness). Figure 8 shows the influence of the bending stiffness variation of the honeycomb core on the morphing profiles for two deflection angles ($\beta = 8°$ and $-6°$). Note that in Figure 8 only the shape of the TE upper skin is drawn emphasizing the changes in morphing profiles. As per the discussion for the actuation force, the cases with lower bending stiffness near the rear spar, *i.e.* Case 9 and Case 10, have larger displacement gradients at the rear spar compared to Case 2 (Figure 8 (b) and (d)). It is clearly seen that the shape of the deformed TE can be tailored using the bending stiffness tailored honeycomb core. The effects of the shape changes on the aerodynamic and aeroacoustic performance of the airfoil is discussed in the next section.
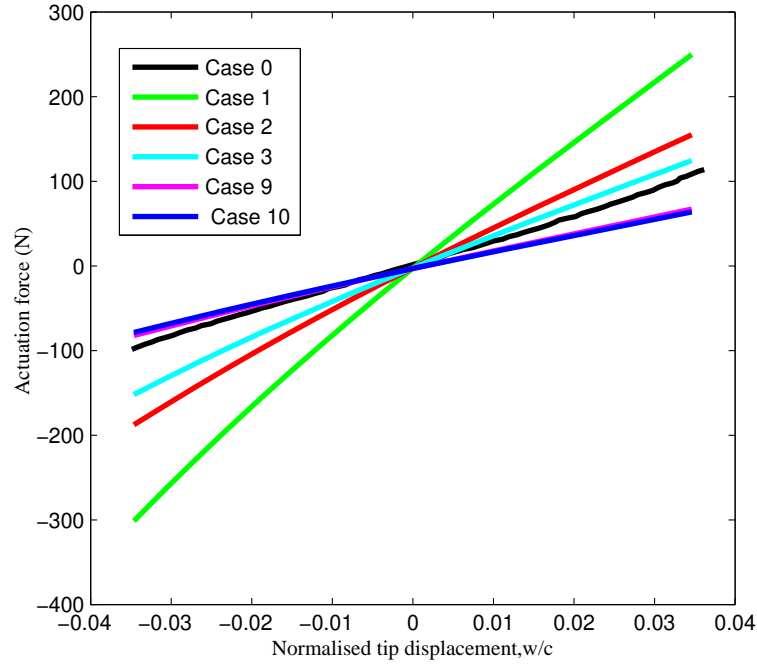

Figure 7. Actuation force requirements of the morphing flaps (Case 0 results from Ref.[4])

## 4.2. Aerodynamic and aeroacoustic performance of the morphing trailing edges

The shapes of the deformed morphing TEs of Case 1 to Case 10 (Table I) at different deflection angles are extracted from the FEM results and interpolated using a MATLAB code for smooth morphing profiles. The geometry of the vertical displacement of Case 0, the morphing flap developed by Daynes *et al.*[4] is defined as a polynomial in terms of the deflection angle β. For the morphing TE of length b, the vertical displacement of the flap, $w(x)$, is defined as a function of the chordwise position, x:[4]

$$w(x) = \varphi(x)\beta,$$

$$\varphi(x) = \begin{cases} 0, & 0 \leq x < c - b \\ \dfrac{(c - x - b)^3}{b^2}, & c - b \leq x < c \end{cases}. \tag{10}$$

where c is the airfoil chord length and b is the morphing TE length (see Figure 1).

With the morphing TE profiles defined above, the aerodynamic coefficients and boundary layer properties of the airfoil can be calculated using Xfoil and the BPM model can then be used to calculate the noise emission. Due to the dipolar
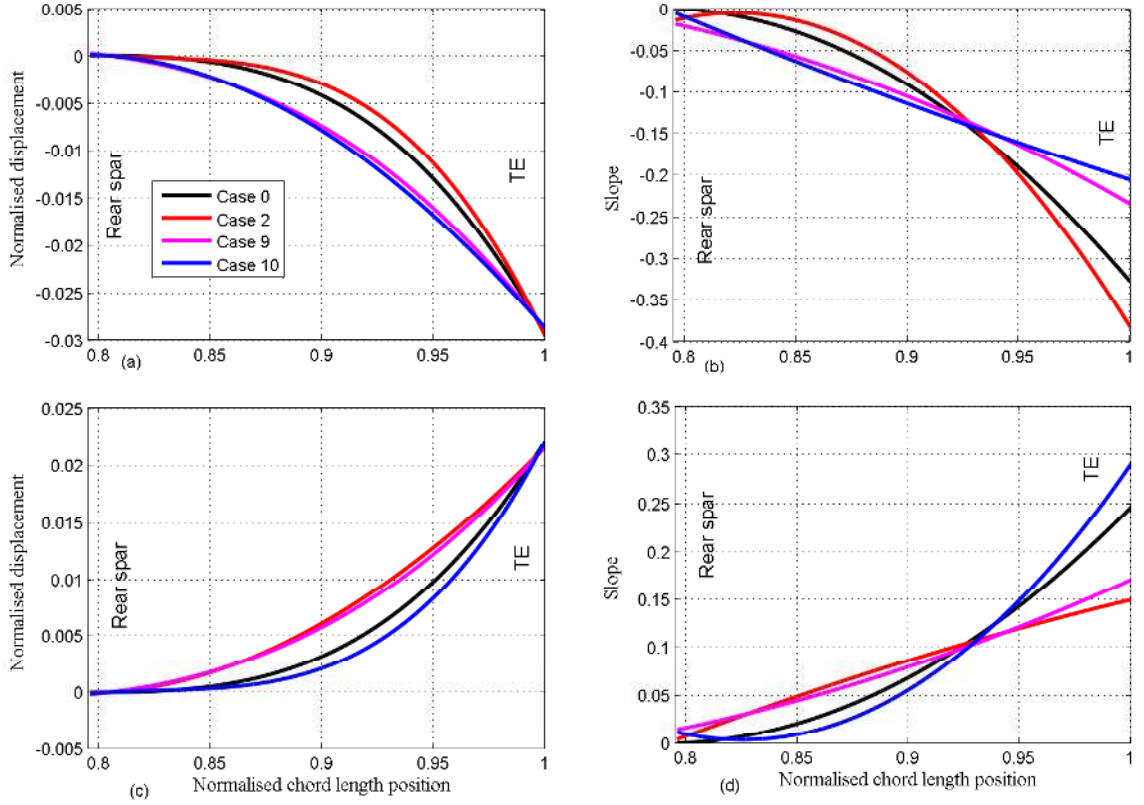
Figure 8. Deformation profiles of Case 0, Case 2, Case 9, Case 10: (a) morphing profiles of the deflection angle $\beta = 8°$; (b) slope of the profiles of of the deflection angle $\beta = 8°$; (c) morphing profiles of the deflection angle $\beta = -6°$; (d) slope of the profiles of of the deflection angle $\beta = -6°$.

nature of airfoil noise, the noise reduction of a rotating frame can be related to that of such a fixed frame,[19] therefore a fixed observer position is chosen where the observer distance r_e is ten times the chord length c and the directivity angles are $\Phi = 90°$ and $\Theta = 90°$ (see Figure 1). In the following sections, the two selected morphing angles, $\beta = 8°$ and $-6°$, are described for effects of downwards and upwards TE deflection on airfoil performance respectively and small angles of attack are chosen due to the effectiveness of tailoring the morphing profiles on low frequency noise emission. Results are shown in Figure 9 to 13.

As shown in Eqs. 1 to 4, the BPM model relies on the boundary layer parameters, *i.e.* the displacement thickness $\delta_{p,s}^*$ at the TE. It is, therefore, important to investigate the effects of tailoring the morphing profiles on the TE boundary layer displacement thickness. Figure 9 presents the changes to the boundary layer thickness on the suction and pressure side, δ_s^* and δ_p^*, of a NACA 63-418 aifoil fitted with morphing TEs with a deflection angle of $\beta = 8°$, morphing length of $b/c = 20\%$, flow velocity of $50m/s$ and angle of attack of $\alpha = 0°$. As shown in Figure 9 (a), due to changes to the morphing profiles, δ_s^* is reduced by 25% as the morphing profiles change from Case 2 to Case 9 and 10, whilst δ_p^* of Case 9 and 10 have increased by 15% compared to Case 2. It can also be seen that the flow behaviour around the morphing TE can be affected by the effective morphing profiles.

The effect of the morphing TE profile on the aerodynamic and aeroacoustic performance of the airfoil is discussed in the section, as shown in Figures 10 to 13. Figure 10 shows the results for a NACA 63-418 airfoil fitted with a morphing TE with an upwards deflection ($\beta = -6°$), morphing length of $b/c = 20\%$, an incoming flow velocity of $50m/s$, and an angle of attack of $\alpha = 0°$. As shown in Figure 10 (a) and (b), compared to Case 0, Morphing cases 9 and 10 present noise reduction of up to 3 dB while Case 2 shows an increase of 1 dB at low frequencies. As expected, at angle of attack of zero degree, an upwards TE deflection can lead to significant lift mitigation compared to downwards TE deflection (Figure 11 to 13) and even negative lift coefficients and lift-to-drag ratios can be achieved (Figure 10 (c) and (d)). With morphing
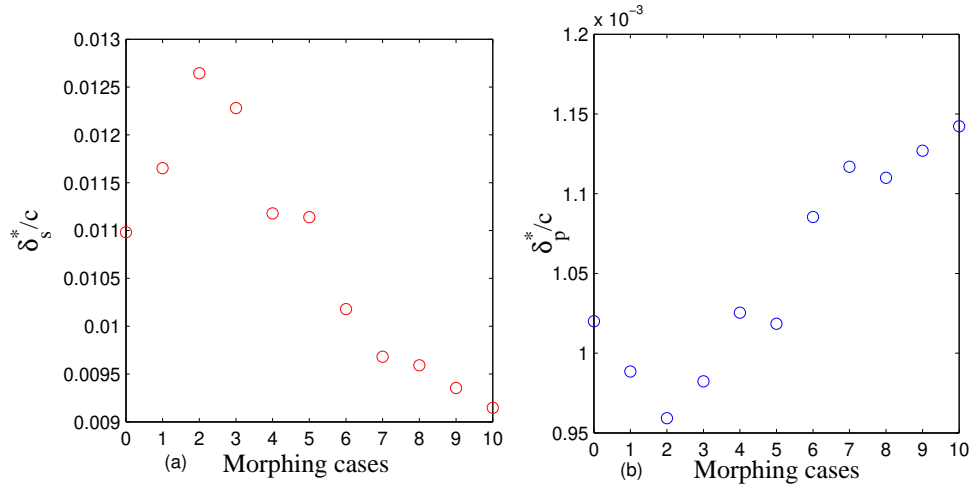
Figure 9. Boundary layer displacement thickness at the trailing edge of a NACA 63-418 airfoil fitted with a morphing flap (deflection angle of $\beta = 8°$, morphing length of $b/c = 20\%$, flow velocity of $50m/s$ and angle of attack of $\alpha = 0°$): (a) the displacement thickness on the suction side; (b) the displacement thickness on the pressure side.

profiles provided by different morphing TE cases, significant changes in lift and drag coefficients and lift-to-drag ratio have been found in this case.

Figure 11 to 13 shows the aerodynamic and aeroacoustic performance of a NACA 63-418 airfoil fitted with morphing flaps with a deflection angle of $\beta = 8°$ (*i.e.*downwards deflection), morphing length of $b/c = 20\%$, a flow velocity of $50m/s$, and angles of attack of $\alpha = 0°, 2°, 3°$, respectively. Similar to Figure 10 (a) and (b), morphing profiles play an important role in the airfoil noise spectra characteristic at small angles of attack (Figure 11 to 13 (a) and (b)). At zero angle of attack (Figure 11 (a) and (b)), Case 9 and 10 present a noise reduction of up to 3 dB compared to Case 0 and Case 2 shows an increase of 2 dB and as the angle of attack increases (Figure 13 (a) and (b)), this effect decreases to 0.5 dB noise reduction with Case 9 and 10 and 1 dB increase with Case 2. This is believed to be mainly due to upstream separation of the flow. As to the aerodynamic performance of the airfoils fitted with different morphing TEs, it has been found that tailoring morphing TE profiles can lead to changes of lift coefficients and lift-to-drag ratios of up to 5% (Figure 11 to 13 (c) and (d)) while the lift-to-drag coefficients remain almost unchanged compared to Case 0.

As discussed earlier, it is found that the morphing TE can significantly affect the lift and drag coefficients, lift-to-drag ratio and low frequency TE noise generation. Fitted with a morphing TE, the shape of the airfoil can be actively changed to adapt to the operation condition, resulting in improvement of aerodynamic and aeroacoustic performance. Results also show that changes to the morphed TE shape using bending stiffness tailored honeycomb cores can significantly affect the TE noise levels at low frequencies at small angles of attack as well as the aerodynamic performance of the airfoil. It is worth adding here that the effectiveness of the novel morphing TE concept can be further improved by increasing the TE length, b/c, which results in extending degree of freedom of morphing TE design and increased potential geometry changes to morphing TE designs. It is also important to note that although the leading edge noise becomes a contributor to the overall noise at low frequencies, trailing edge noise also remains a significant noise generation mechanism. As mentioned by Kinzie *et al*,[51] several acoustic measurement campaigns[21,52] have established that turbulent boundary layer trailing edge noise is the dominant mechanism for large wind turbines. The significance of inflow-turbulence noise contribution to the overall sound level of large wind turbines is still an open issue and requires more research.[53]

5. CONCLUDING REMARKS

Shape adaptable structures, such as a morphing TE, have received growing attention for their perceived advantages over traditional mechanical airfoil control surfaces. In this paper, following the idea of airfoil shape optimization, a novel morphing TE using a bending stiffness tailored honeycomb core with ZPR is investigated for airfoil noise and flow control purposes. A NACA 63-418 airfoil of chord $1.3m$ was chosen and fitted with the morphing TE. A two dimensional ABAQUS FEM is developed to predict the deflection shapes of the flap and the aerodynamic and aeroacoustic performance are calculated using Xfoil and the BPM model. In order to study the effect of the changes to the shape of the morphed TE on
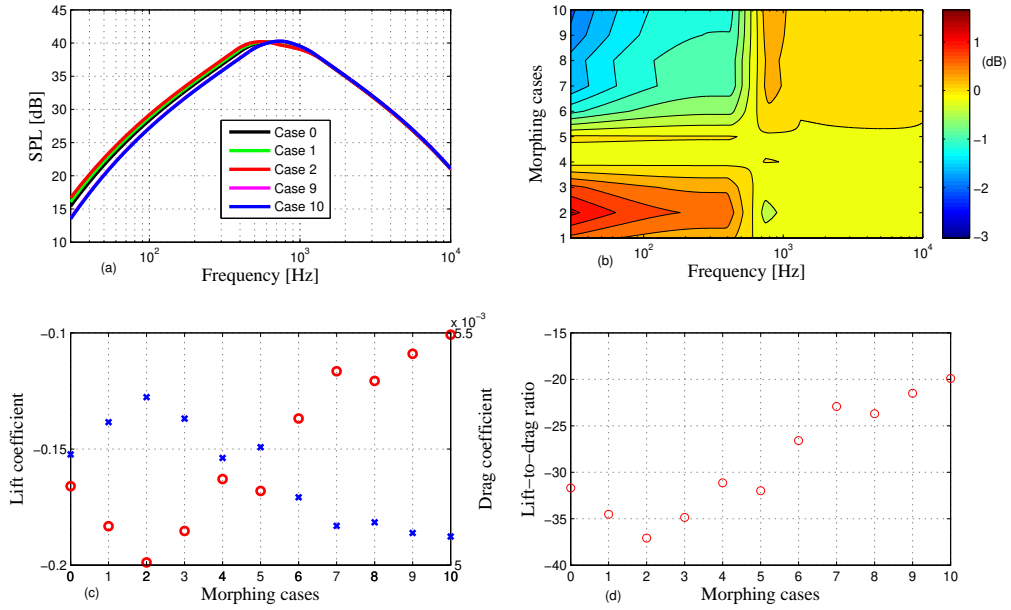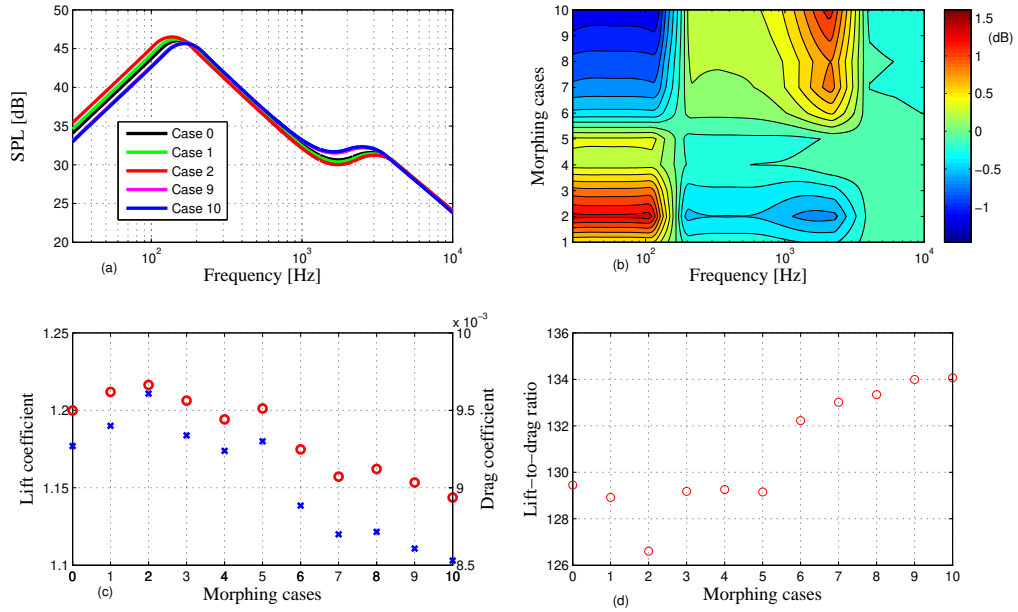
Figure 10. Results of a NACA 63-418 airfoil with a morphing trailing edge (morphing length of $b/c = 20\%$, deflection angle of $\beta = -6°$, flow velocity of $50m/s$ and angle of attack of $\alpha = 0°$): (a). the SPL of the airfoil; (b). contour plot of noise reduction relative to Case 0; (c). lift and drag coefficients: the cross line represents the drag coefficient and the circle line is the lift coefficient; (d). lift-to-drag ratio.
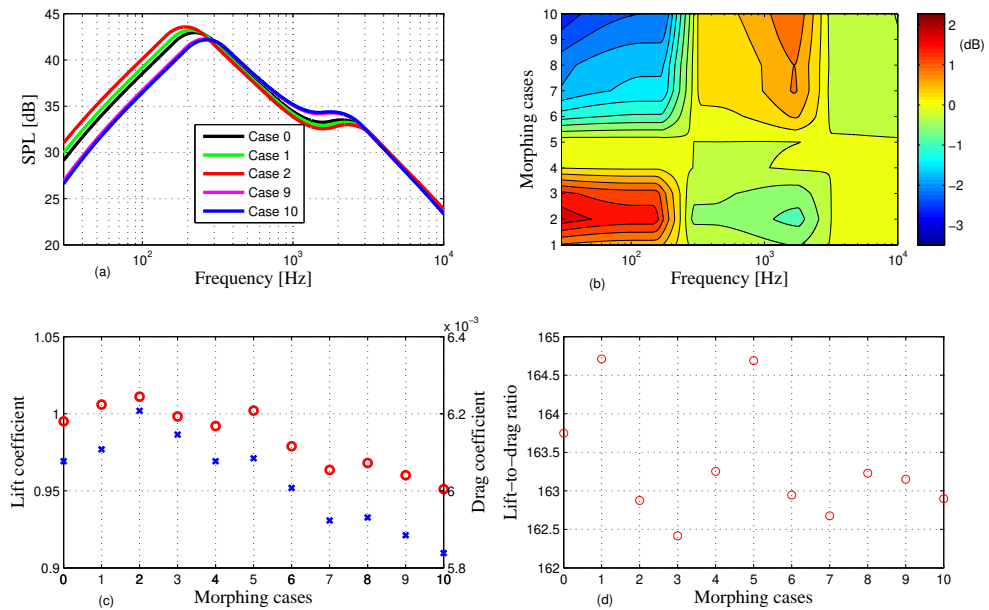
Figure 11. Results of a NACA 63-418 airfoil with a morphing trailing edge (morphing length of $b/c = 20\%$, deflection angle of $\beta = 8°$, flow velocity of $50m/s$ and angle of attack of $\alpha = 0°$): (a). the SPL of the airfoil; (b). contour plot of noise reduction relative to Case 0; (c). lift and drag coefficients: the cross line represents the drag coefficient and the circle line is the lift coefficient; (d). lift-to-drag ratio.

noise level and aerodynamic efficiency, 10 different honeycomb core designs were chosen for a preliminary optimization design. It is found that flow boundary layer behaviour can be significantly affected by tailoring the profiles of deformed

;

Figure 12. Results of a NACA 63-418 airfoil with a morphing trailing edge (morphing length of $b/c = 20\%$, deflection angle of $\beta = 8°$, flow velocity of $50 m/s$ and angle of attack of $\alpha = 2°$): (a). the SPL of the airfoil; (b). contour plot of noise reduction relative to Case 0; (c). lift and drag coefficients: the cross line represents the drag coefficient and the circle line is the lift coefficient; (d). lift-to-drag ratio.
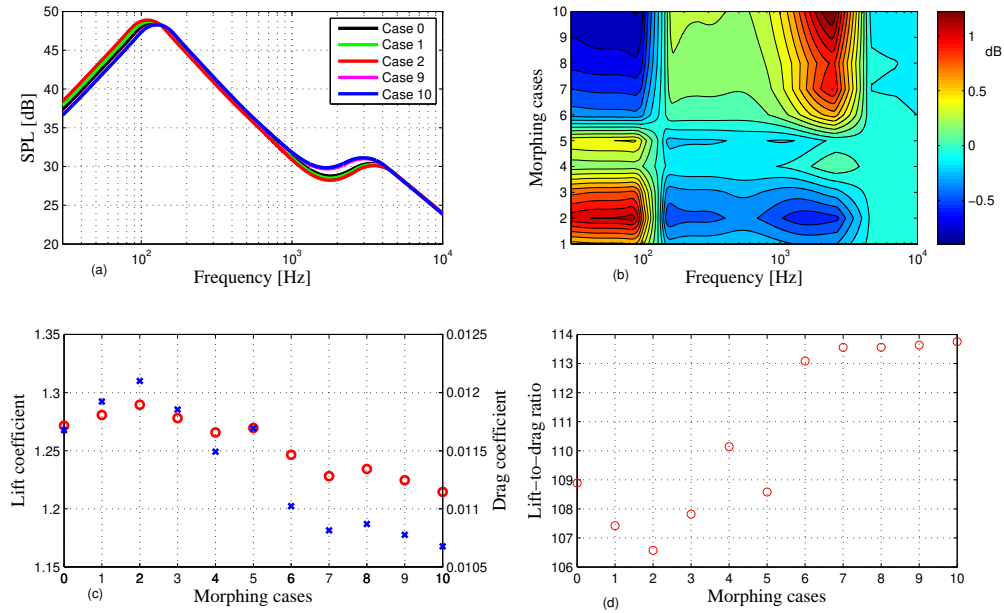
Figure 13. Results of a NACA 63-418 airfoil with a morphing trailing edge (morphing length of $b/c = 20\%$, deflection angle of $\beta = 8°$, flow velocity of $50 m/s$ and angle of attack of $\alpha = 3°$): (a). the SPL of the airfoil; (b). contour plot of noise reduction relative to Case 0; (c). lift and drag coefficients: the cross line represents the drag coefficient and the circle line is the lift coefficient; (d). lift-to-drag ratio.

morphing TE, resulting in different TE noise levels. Results show that at small angles of attack, noise reduction of up to 3 dB and increase of 2 dB can be achieved by tailoring the morphing profiles while the lift coefficient and lift-to-drag ratio are not affected.

To better understand the trailing-edge noise generation and also the noise reduction mechanism using the morphing trailing-edge, further research, such as unsteady CFD, is needed to study the effects of surface profile on the unsteady surface pressure fluctuations and the far-field noise. Experiments are necessary in future to better understand the flow behaviour and noise reduction mechanism associated with morphing TE. Future work could include:

- manufacture of the bending stiffness tailored honeycomb core and constructing of the morphing flap to investigate the in-service effects, such as maintenance, actuation loads and fatigue life;
- experimental studies to understand the flow control and noise reduction mechanisms;
- optimization design of the flap concept based on the working conditions of the wind turbine;
- aeroelasticity analysis of the morphing flap.

ACKNOWLEDGEMENT

REFERENCES

1. Kaldellis J.K, Zafirakis D. The wind energy (r)evolution: A short review of a long history. *Renewable Energy* 2011; **36**:1887-1901. DOI: 10.1016/j.renene.2011.01.002.
2. Johnson S.J, Baker J.P, van Dam C.P, Berg D. An overview of active load control techniques for wind turbines with an emphasis on microtabs. *Wind Energy* 2009 ;**13**:239-253.DOI: 10.1002/we.356.
3. Wolff T, Ernst B, Seume J.R. Aerodynamic behaviour of an airfoil with morphing trailing edge for wind turbine applications. *The Science of Making Torque from Wind 2014* ; 18-20 June 2014, Copenhagen, Denmark. DOI:10.1088/1742-6596/524/1/012018.
4. Daynes S, Weaver P. A morphing trailing edge device for a wind turbine. *Journal of Intelligent Material Systems and Structures* 2012; **23**: 691-701. DOI:10.1177/1045389X12438622.
5. Daynes S, Weaver P. Design and testing of a deformable wind turbine blade control surface. *Smart Materials and Structures* 2012; **21**:105019-105029. DOI:10.1088/0964-1726/21/10/105019.
6. Straub F.K, Ngo H.T, Anand V, Domzalski D.B. Development of a piezoelectric actuator for trailing edge flap control of full scale rotor blade. *Smart Materials and Structures* 2001 ;**10**:25-34. doi:10.1088/0964-1726/10/1/303.
7. Bergami L, Riziotis V.A, Gaunaa M. Aerodynamic response of an airfoil section undergoing pitch motion and trailing edge flap deflection: a comparison of simulation methods. *Wind Energy* 2014; Early Version, DOI: 10.1002/we.1759
8. Bergami L, Poulsen N.K. A smart rotor configuration with linear quadratic control of adaptive trailing edge flaps for active load alleviation. *Wind Energy* 2014; **18**:625-641, DOI: 10.1002/we.1716
9. Andersen P.B, Henriksen L, Gaunaa M, Bak C, Buhl T. Deformable trailing edge flaps for modern megawatt wind turbine controllers using strain gauge sensors. *Wind Energy* 2010; **13**:193-206, DOI: 10.1002/we.371
10. Heinz J, Sorensen N.N, Zahle F. Investigation of the load reduction potential of two trailing edge flap control using CFD. *Wind Energy* 2011;**14**:449-462.DOI: 10.1002/we.435.
11. Hulskamp A.W, van Wingerden J.W, Barlas T, Champliaud H, van Kuik G.A.M, Bersee H.E.N, Verhaegen M. Design of a scaled wind turbine with a smart rotor for dynamic load control experiments. *Wind Energy* 2011 ;**14**:339-354.DOI: 10.1002/we.424
12. Wolf A, Lutz T, Wurz W, Kramer E, Stalnov O, Seifert A. Trailing edge noise reduction of wind turbine blades by active flow control. *Wind Energy* 2014.DOI: 10.1002/we.1737.
13. Wagner S, Bareriss R, Guidati G. *Wind Turbine Noise*; Springer:Berlin,1996;67-92.
14. Brooks T, Pope D, Marcolini M. *Airfoil self-noise and prediction*; NASA RP-1218, 1989.
15. Marsden AL, Wang M, Dennis JE, Moin P. Trailing edge noise reduction using derivative-free optimization and large-eddy simulation. *Journal of Fluid Mechanic* 2007; **572**:13-36. DOI:10.1017/S0022112006003235.
16. Moriarty PJ, Guidati G, Migliore P. Prediction of turblent inflow and trailing-edge noise for wind turbine. *11th AIAA/CEAS Aeroacoustics Conference (26th AIAA Aeroacoustics Conference)*; 23-25 May 2005, Monterey, California, USA. DOI: 10.2514/6.2005-2881.
17. Azarpeyvand M, Gruber M, Joseph PF. An analytical investigation of trailing edge noise reduction using novel serrations. *19th AIAA/CEAS Aeroacoustic Conference*, Berlin, German, 27-29, May 2013. DOI: 10.2514/6.2013-2009.

18. Gruber M., Azarpeyvand M, Joseph PF. Airfoil trailing edge noise reduction by the introduction of sawtooth and slitted trailing edge geometries. *Proceedings of 20th International Congress on Acoustics*; Sydney, Australia ,23-27 August 2010.

19. Sinayoko S, Azarpeyvand M, Lyu B. Trailing edge noise prediction for rotating serrated blades. *20th AIAA/CEAS Aeroacoustics Conference*, Atlanta, GA. 16-20 June 2014.

20. Howe MS . Noise produced by a sawtooth trailing edge. *The Journal of Aeroacoustical Sciety of America* 1991; **90**:482-487. DOI:10.1121/1.401273.

21. Oerlemans S, Fisher M, Maeder T, Kogler K. Reduction of wind turbine noise using optimized airfoils and trailing-edge serrations. *AIAA Journal* 2009; **47**:1470-1481. DOI: 10.2514/1.38888.

22. Herr M, Dobrzynski W. Experimental investigations in low noise trailing-edge design. *AIAA Journal* 2005; **43**:1167-1175. DOI: 10.2514/1.11101.

23. Finez A, Jondeau E, Roger M, Jacob MC. Broadband noise reduction with trailing edge brushes. *16th AIAA/CEAS Aeroacoustics Conference*, Stockholm, Sweden, 2010. DOI:10.2514/6.2010-3980.

24. Howe MS. On the added mass of a perforated shell, with application to the generation of aerodynamic sound by a perforated trailing edge. *Proceedings of the Royal Society A: Mathematical,Physical and Engineering Science*1979; **365**: 209-233. DOI: 10.1098/rspa.1979.0014

25. Geyer T, Sarradj E, Fritzsche C. Measurements of the noise generation at the trailing edge of porous airfoils. *Experiments in Fluids* 2010; **48**:291-308. DOI:10.1007/s00348-009-0739-x.

26. Gocmen T, Ozerdem B. Airfoil optimization for noise emission problem and aerodynamic performance criterion on small scale wind turbines. *Energy* 2012; **41**:62-71. DOI:10.1016/j.energy.2012.05.036.

27. Jones BR, Crossley WA, Lyrintzis AS. Aerodynamic and aeroacoustic optimization of rotorcraft airfoils via a parallel genetic algorithms. *Journal of Aircraft* 2000; **37**:1088-1096. DOI:10.2514/2.2717.

28. Gad-el-Hak M. *Flow Control: Passive, Active, and Reactive Flow Management*; Cambridge University Press: New York, 2006.

29. Koreanschi A, Sugar-Gabor O, Botez R. M. New numerical study of boundary layer behaviour on a morphing wing-with-aileron system, *32nd AIAA Applied Aerodynamics Conference, AIAAs Aviation 2014*, 16-20 June, 2014, Atlanta, United States.

30. Thill C, Etches J, Bond I, Potter K, Weaver P. Morphing skins. *The Aeronautical Journal* 2008; **112**:117-139.

31. Lachenal X, Daynes S, Weaver P. Review of morphing concepts and materials for wind turbine blade applications. *Wind Energy* 2013; **16**: 283-307. DOI: 10.1002/we.531.

32. Chopra I. Review of state of art of smart structures and integrated systems. *AIAA Journal* 2002; **40**:2145-2187. DOI: 10.2514/2.1561.

33. Campanile LF. *Adaptive Structures: Engineering Applications* (Wagg D, Bond IP, Weaver PM, Friswell MI, eds). Wiley:Chichester, 2007. Chapter 4: Lightweight Shape-adaptable Airfoils: A New Challenge for an Old Dream.

34. Bartley-Cho JD, Wang DP, Martin CA, Kudva JN, West MN. Development of high-rate, adaptive trailing edge control surface to the smart wing phase 2 wind tunnel model. *Journal of Intelligent Material Systems and Structures* 2004; **15**: 279-291. DOI:10.1177/1045389X04042798.

35. Gibson LJ, Ashby MF. *Cellular Solids: structure and properties*, 2nd edn. Cambridge University Press:New York, 1997; 93-172.

36. Olympio KR, Gandhi F. Zero Poisson's ratio cellular honeycombs for flex skins undergoing one-dimensional morphing. *Journal of Intelligent Material Systems and Structures* 2010;**21**:1737-1753. DOI: 10.1177/1045389X09355664.

37. Olympio KR, Gandhi F. Flexible skins for morphing aircraft using cellular honeycomb cores.*Journal of Intelligent Material Systems and Structures* 2009; **21**:1719-1735. DOI:10.1177/1045389X09350331.

38. Bubert EA, Woods B KS, Lee K, Kothera CS, Wereley NM. Design and fabrication of a passive 1D morphing aircraft skin. *Journal of Intelligent Material Systems and Structures* 2010, **21**:1699-1717. DOI:10.1177/1045389X10378777.

39. Chen Y, Scarpa F, Remillat C, Farrow I, Liu Y, Leng J. Curved kirigami SILICOMB cellular structures with zero Poisson's ratio for large deformation and morphing. *Journal of Intelligent Material System and Structures* 2013;**25**:731-743; DOI:10.1177/1045389X13502852.

40. Drela M, Youngren H. *Xfoil 6.8 User Primer*; Massachusetts Institute of Technology, Cambridge, Massachusetts, 2001.

41. Schlinker R, Amiet R. *Helicopter rotor trailing edge noise*; NASA-CR-3470,1981.

42. Herrig A, Kamruzzamam M, Wurz W, Wagner S. Broadband airfoil trailing-edge noise prediction from measured surface pressures and spanwise length scales. *International Journal of Aeroacoustics* 2013; **12**:53-82. DOI:10.1260/1475-472X.12.1-2.53.

43. Wang M,. Moreau S, Iaccarino G, Roger M. LES prediction of wall-pressure fluctuation and noise of a low-speed airfoil. *International Journal of Aeroacoustics* 2009; **8**:177-198. DOI:10.1121/1.2934513.

44. Imamura T, Enomoto S, Kazuomi Yamamoto. Noise simulation around NACA0012 wingtip using large-eddy-simulation. *Transactions of the Japan Society for Aeronautical and Space Sciences* 2013;**55**:214-221. DOI:10.2322/tjsass.55.214.

45. DeGennaro M, Kuehnelt H, Simos TE, Psihoyios G, Tstouras C, Anastassi Z. Semi-empirical modelling of broadband noise for aerofoils. *Numerical Analysis and Applied Mathematics ICNAAM 2011 AIP Conference Proceedings* 2011; **1389**:1498-1502. DOI:1498-1502.10.1063/1.3637909.

46. Wolf WR, Lele SK. Trailing edge noise prediction using compressible large eddy simulation and acoustic analogy. *AIAA Journal* 2012; **50**:2423-2434. DOI:10.2514/1.J051638.

47. Young WC, Budynas RG. *Roark's formulas for stress and strain* 7th edn, McGraw-Hill: New York, 2002.

48. Lira C, Scarpa F. Transverse shear stiffness of thickness gradient honeycombs. *Composites Science and Technology* 2010; **70**: 930-936. DOI:10.1016/j.compscitech.2010.02.007.

49. Jones RM. *Mechanics of composite materials* 2nd edn; Taylor and Francis:Philadelphia, 1999; 190-202.

50. Bertagnolio F, Sorensen N, Johansen J, Fuglsang P. *Wind Turbine Airfoil Catalogue*; Riso-R-1280(EN), 2001.

51. Kinzie K, Drobietz R, Petijiean B, Honhoff S. *Concepts for Wind Turbine Sound Mitigation*; AWEA Windpower, 2013.

52. Oerlemans S, Sijtsma P, Mendez Lopez B. Location and quantification of noise sources on a wind turbine. *Journal of Sound and Vibration* 2007; **299**:869-883.doi:10.1016/j.jsv.2006.07.032.

53. Guidati G, Ostertag J, Wagner S. Prediction and reduction of wind turbine noise: an overview of research activities in Europe. *2000 ASME Wind Energy Symposium*, AIAA Paper 2000-0042, 2000.